PCCP

PAPER

View Article Online
View Journal | View Issue

Cite this: *Phys. Chem. Chem. Phys.*, 2024, **26**, 14037

Difference in reaction mechanism between $ZnZrO_x$ and $InZrO_x$ for CO_2 hydrogenation†

Shohei Tada, *[a] Yurika Ogura,[b] Motohiro Sato,[c] Akihiro Yoshida,[cd] Tetsuo Honma,[e] Masahiko Nishijima,[f] Tatsuya Joutsuka *[g] and Ryuji Kikuchi *[a]

Received 13th February 2024,
Accepted 19th April 2024

DOI: 10.1039/d4cp00635f

rsc.li/pccp

Oxide solid-solution catalysts, such as Zn-doped ZrO_2 ($ZnZrO_x$) and In-doped ZrO_2 ($InZrO_x$), exhibit distinctive catalytic capabilities for CH_3OH synthesis *via* CO_2 hydrogenation. We investigated the active site structures of these catalysts and their associated reaction mechanisms using both experimental and computational approaches. Electron microscopy and X-ray absorption spectroscopy reveal that the primary active sites are isolated cations, such as Zn^{2+} and In^{3+}, dissolved in tetragonal ZrO_2. Notably, for Zn^{2+}, decomposition of the methoxy group, which is an essential intermediate in CH_4 synthesis, is partially suppressed because of the relatively high stability of the methoxy group. Conversely, the methyl group strongly adsorbs on In^{3+}, facilitating the conversion of the methoxy species into methyl groups. The decomposition of CH_3OH is also suggested to contribute to CH_4 synthesis. These results highlight the generation of CH_4 as a byproduct of the $InZrO_x$ catalyst. Understanding the active site structure and elucidating the reaction mechanism at the atomic level are anticipated to contribute significantly to the future development of oxide solid-solution catalysts.

Introduction

Carbon dioxide hydrogenation is recognized as a key technology for the utilization of CO_2. Hydrogen is generated by water electrolysis using renewable energy sources. The produced H_2 reacts with CO_2 to create raw materials for chemicals and fuels. This process has the potential to contribute substantially to the establishment of a sustainable society, provided the feasibility of obtaining cost-effective H_2 is considered. Methanol is often regarded as the building block in C1 chemistry. Essentially, CO_2-to-CH_3OH hydrogenation (eqn (1)) occurs at approximately 250 °C using Cu-based catalysts, such as $Cu/ZnO/Al_2O_3$,[1–3] and the resulting CH_3OH molecules are subsequently transformed into hydrocarbons and oxygenates at acid sites in solid acid catalysts at 400 °C and higher temperatures.[4] When reactors designed for CH_3OH synthesis and conversion reactions are connected in series, it is essential to recognize that the former reaction typically determines the overall rate. In the context of CO_2 hydrogenation, additional challenges arise owing to the simultaneous formation of CO byproducts through the reverse water gas shift reaction (eqn (2)) and/or CH_3OH decomposition (eqn (3)), along with the CH_3OH synthesis reaction. Thermodynamically, the dominance of CO byproducts occurs under conditions where the reaction temperature is high.[5] Furthermore, depending on the catalyst, CH_4 by-production *via* CO_2 methanation (eqn (4)) may also occur. To enhance the efficiency of the entire system, it is necessary to improve the yield of CH_3OH.

$$CO_2 + 3H_2 \rightarrow CH_3OH + H_2O \quad (1)$$

$$CO_2 + H_2 \rightarrow CO + H_2O \quad (2)$$

$$CH_3OH \rightarrow CO + 2\,H_2 \quad (3)$$

$$CO_2 + 4H_2 \rightarrow CH_4 + 2H_2O \quad (4)$$

To address this limitation, numerous researchers have explored bifunctional catalysts that incorporate both the CH_3OH synthesis and conversion reactions. These catalysts facilitate both reactions simultaneously in a one-pass process:

[a] *Division of Applied Chemistry, Graduate School of Engineering, Hokkaido University, Sapporo, Hokkaido 060-8628, Japan. E-mail: shohei.tada.st@eng.hokudai.ac.jp, rkikuchi8@eng.hokudai.ac.jp*
[b] *Department of Materials Science and Engineering, Ibaraki University, 4-12-1, Nakanarusawa, Hitachi, Ibaraki 316-8511, Japan*
[c] *Graduate School of Science and Technology, Hirosaki University, 3 Bunkyo-cho, Hirosaki, Aomori 030-8651, Japan*
[d] *Institute of Regional Innovation, Hirosaki University, 3 Bunkyo-cho, Hirosaki, Aomori 030-8651, Japan*
[e] *Japan Synchrotron Radiation Research Institute, Sayo-gun, Hyogo 679-5198, Japan*
[f] *Flexible 3D System Integration Laboratory, Osaka University, 8-1 Mihogaoka Ibaraki-Shi, Osaka 567-0047, Japan*
[g] *Department of Materials Science and Engineering, Ehime University, 3 Bunkyo-cho, Matsuyama, Ehime 790-8577, Japan. E-mail: joutsuka.tatsuya.zk@ehime-u.ac.jp*

† Electronic supplementary information (ESI) available. See DOI: https://doi.org/10.1039/d4cp00635f

the CH_3OH produced is swiftly intercepted by a solid acid catalyst, generating hydrocarbons and oxygenates and effectively suppressing CO byproducts. Notably, integrating CH_3OH synthesis catalysts with solid acid catalysts substantially enhances the overall yield of CH_3OH-derived products, including CH_3OH, hydrocarbons, and oxygenates.[6] However, the considerable difference between the reaction temperatures of these two processes poses a challenge. Thus, optimization of the catalyst design involves either increasing the temperature for CH_3OH synthesis or reducing the temperature for CH_3OH conversion.

Metal-oxide catalysts have emerged as promising agents for CO_2-to-CH_3OH hydrogenation. Notably, CH_3OH synthesis over these catalysts occurs at higher temperatures (above 300 °C) than over traditional Cu-based catalysts. The combination of metal oxides and solid acid catalysts enables the one-pass hydrogenation of CO_2 to hydrocarbons and oxygenates. Some reported metal oxide catalysts for high-temperature CH_3OH synthesis include Zn-doped ZrO_2,[7–13] In-doped ZrO_2,[14,15] In_2O_3,[14–16] and Ga-doped ZrO_2,[17] among others. For Zn-doped ZrO_2, isolated [ZnO_a] clusters activate H_2 molecules, whereas Zr^{4+} sites activate CO_2, emphasizing the crucial role of the interfacial sites between Zn and Zr in high-temperature CH_3OH synthesis.[8] This reaction over Zn-doped ZrO_2 proceeds *via* a formate route, where the surface formate species on the Zr^{4+} sites serve as essential intermediates, eventually hydrogenating to methoxy species on Zr^{4+} and CH_3OH.[7,8,12] In the case of In_2O_3, as initially reported by Ye *et al.*,[18] the reaction over In_2O_3-based catalysts is expected to follow the formate route.[18–21] However, the mechanism of In_2O_3-based catalysts appears to be slightly different from that of Zn-doped ZrO_2 because In_2O_3-based catalysts produce a small amount of CH_4, unlike Zn-doped ZrO_2.[22] Our study aimed to investigate the differences between the Zn-doped ZrO_2- and In_2O_3-based catalysts. Similar to traditional methanation catalysts, the catalyst may undergo CO_2 methanation, in which a surface formate species is hydrogenated to CO and the resulting CO is then methanated.[23,24] Alternatively, the surface methoxy species or adsorbed CH_3OH molecules may be directly hydrogenated to CH_4.[25] In this study, we prepared model catalysts of Zn- and In-doped ZrO_2 and examined the differences in their reaction mechanisms.

Experimental

Chemicals

Amorphous ZrO_2 was supplied by Daiichi Kigenso Kagaku Kogyo (product name: NND). $Zn(NO_3)_2{\cdot}6H_2O$, ZnO, In_2O_3, and quartz sand were purchased from Fujifilm Wako. $In(NO_3)_3{\cdot}nH_2O$ was purchased from Kanto Chemical.

Catalyst preparation

$ZnZrO_x$ and $InZrO_x$ were prepared using an incipient wetness impregnation method. The amorphous ZrO_2 was impregnated with a metal nitrate aqueous solution, dried at 110 °C for 12 h, and calcined at 500 °C for 3 h. The abbreviations and compositions of the prepared catalysts are summarized in Table 1.

Table 1 Abbreviation, composition, specific surface area, and total pore volume of $ZnZrO_x$ and $InZrO_x$

Catalyst	Abbreviation	Zn/Zr molar ratio[a] [−]	In/Zr molar ratio[a] [−]	SSA[b] [$m^2\ g^{-1}$]	Vm[c] [$10^{-2}\ cm^3\ g^{-1}$]
$ZnZrO_x$	ZnZr46	0.46		40	0.14
$InZrO_x$	InZr09		0.087	82	0.24
	InZr22		0.22	66	0.15

[a] Determined by XRF. [b] Specific surface area determined by N_2 adsorption. [c] Total pore volume determined by N_2 adsorption. p/p_0 = 0.98.

Characterization

X-ray fluorescence (XRF), X-ray diffraction (XRD), N_2 adsorption and desorption, X-ray absorption spectroscopy (XAS), and scanning transmission electron microscopy (STEM) analyses were performed. The detailed procedure is summarized in the ESI.†

Performance test

CO_2 hydrogenation. A stainless-steel fixed-bed tubular reactor was used for CO_2 hydrogenation performance tests. Each catalyst was compressed at 20 MPa to form tablets. The tablet was crushed and sieved to obtain catalyst grains of 1.18–1.7 mm. The grains (300 mg) were placed in the catalyst bed. The reaction temperature was controlled using a K-type thermocouple inserted into the catalyst bed, and an electric furnace installed outside the catalyst bed. A reaction gas mixture (CO_2/H_2/N_2 = 1/3/1) was introduced into the catalyst bed at a flow rate of 30 $mL_{STP}\ min^{-1}$. The reaction pressure was set to 1.0 MPa because it is restricted to 1.0 MPa by the High-Pressure Gas Safety Act of Japan. The outlet gas composition was analyzed using a gas chromatograph (SHIMADZU GC-2014) with a thermal conductivity detector (TCD) and flame ionization detector (FID). According to eqn (5)–(7), the CO_2 conversion, space-time yield of species i [$mL\ min^{-1}\ g^{-1}$], and yield of species i were obtained.

$$\mathrm{CO_2\ conversion} = \frac{F_{\mathrm{in,CO_2}} - F_{\mathrm{out,CO_2}}}{F_{\mathrm{in,CO_2}}} \quad (5)$$

$$\mathrm{Space-time\ yield\ of}\ i\ \mathrm{species} = \frac{F_{\mathrm{out},i}}{w} \quad (6)$$

$$\mathrm{Yield\ of}\ i\ \mathrm{species} = \frac{F_{\mathrm{out},i}}{F_{\mathrm{in,CO_2}}} \quad (7)$$

In these equations, $F_{\mathrm{in},i}$ and $F_{\mathrm{out},i}$ are the inlet and outlet gas flow rates of species i [$mL_{STP}\ min^{-1}$], respectively, and w is the catalyst weight [g]. The carbon yield was 100% ± 0.5%.

Methanol decomposition. A silicate glass fixed-bed tubular reactor (i.d. 7.5 mm) was used for CH_3OH decomposition performance tests. Each catalyst was compressed at 25 MPa to form tablets. The tablet was crushed and sieved to obtain catalyst grains of 0.85–1.4 mm. Grains (500 mg) were placed in a catalyst bed. The reaction temperature was controlled using a K-type thermocouple, which was inserted into the catalyst bed,

and an electric furnace was installed outside the catalyst bed. Liquid CH_3OH, supplied by a high-performance liquid chromatography pump (SHIMADZU LC-20AT) with a constant flow rate (0.038 mL min^{-1} as a liquid, corresponding to 21.06 mL_{STP} min^{-1} as a gas), was introduced into a vaporizer heated at 130 °C with N_2 (flow rate: 110 mL_{STP} min^{-1}) and H_2 (flow rate: 38 mL_{STP} min^{-1}) streams. The gas mixture was fed into the catalyst bed. The reaction was conducted under atmospheric pressure. The outlet gas composition was analyzed using gas chromatographs equipped with a TCD (SHIMADZU GC-8A) for CO quantification and an FID (SHIMADZU GC-2014) for CH_4 and dimethyl ether (CH_3OCH_3) quantification. According to eqn (8), the space-time yield of the product of species i (CH_4, CO, and CH_3OCH_3) was obtained.

$$\text{Space} - \text{time yield of } i \text{ species} = \frac{F_{\text{out},i} \times N}{w} \quad (8)$$

where $F_{\text{out},i}$ is the outlet gaseous flow rate of i species [mL_{STP} min^{-1}], and N is the number of carbon atoms in a molecule of each product.

Calculation. We performed spin-polarized density functional theory (DFT) calculations using the vienna *ab initio* simulation program,[26,27] which adopts the projector-augmented wave method.[28] We used the generalized-gradient approximation for DFT calculations with the Perdew–Burke–Ernzerhof[29] exchange–correlation functional. The plane-wave cutoff was 400.0 eV unless otherwise noted. The total energy for each self-consistent field step converged to an accuracy of 10^{-5} eV. Gaussian smearing was used with a width of 0.1 eV.

We calculated the electronic energy under 3D periodic boundary conditions. The optimization of a unit cell of bulk tetragonal (t)-ZrO_2 results in cell lengths of $a = b = 3.623$ Å and $c = 5.280$ Å using a larger plane-wave cutoff of 600.0 eV, which agrees with previous studies.[30,31] The initial configuration of the t-ZrO_2 (101) surface was made by cleaving the optimized bulk ZrO_2. Along the surface parallel direction, the cell lengths are 12.806 Å × 10.868 Å, and the employed Monkhorst–Pack[32] k-point mesh is 2 × 2. Along the surface normal direction, the cleaved surface has two ZrO_2 layers (72 atoms) to follow the computational model in ref. 31 because ref. 31 (two-layer model) and ref. 7 (three-layer model) yielded comparable energy profiles (the validity of our model is discussed in the ESI†); the width of the vacuum region is 15 Å, and one k-point is used. During the geometry optimization, the coordinates of the atoms, except for the bottom layer, were optimized. An electric dipole correction was considered.[33]

The $InZrO_x$ surface was prepared by removing one O atom and replacing one Zr atom with an In atom from the top layer of a stoichiometric ZrO_2 surface. The Zr atoms on the surface are classified into two types, and the replaced Zr atom acts as a strong Lewis site with longer Zr–O bonds.[34,35] Fig. S1 (ESI†) shows the positions of In and one oxygen vacancy (V_O). For comparison, $ZnZrO_x$ was prepared using the same method. The V_O was situated next to the In atom, similar to a previous study of the $ZnZrO_x$ surface.[31] The geometries of the surfaces were optimized, and the adsorbates were placed on the optimized surfaces. The adsorption energies are calculated using the following eqn (9):

$$E_{\text{ads}} = E(\text{substrate} + \text{adsorbate}) - E(\text{substrate}) - E(\text{adsorbate}) \quad (9)$$

where E(substrate + adsorbate), E(substrate), and E(adsorbate) are the energies of the adsorbed complex, the substrate, and the adsorbate, respectively. According to this definition, a lower adsorption energy indicates stable adsorption.

The climbing-image nudged elastic band method[36] was used to calculate the potential surface and activation energies. Free energy (G) was computed using the normal mode analysis. In the calculations of the translational, rotational, and vibrational enthalpic and entropic contributions, the gas-phase molecules were approximated as ideal gases. The further details are summarized in the ESI.†

Results and discussion

CO_2 hydrogenation

We conducted CO_2 hydrogenation performance tests using ZnZr46, InZr9, and InZr22. We have previously reported that the Zn/Zr ratio of $ZnZrO_x$ does not affect its catalytic performance on CO_2-to-CH_3OH hydrogenation. Therefore, this time, we adopted ZnZr46 as a representative $ZnZrO_x$.[8] Fig. S2 (ESI†) shows plots of CO_2 conversion at different reaction temperatures. At 250 °C, CO_2 conversion is approximately 1%, irrespective of the catalyst type. For ZnZr46, the CO_2 conversion gradually increases from 1% to 4% with increasing reaction temperature. For InZr09 and InZr22, the increase in CO_2 conversion is more substantial. Particularly, at 325 °C, the CO_2 conversion for InZr09 and InZr22 is more than twice as high as that of ZnZr46, reaching 8%.

Fig. 1 illustrates the space-time yields (STY) of CH_3OH, CO, and CH_4 for ZnZr46, InZr09, and InZr22, with the right axes indicating the yields. In this experiment, the identified carbon-containing products are limited to CH_3OH, CO, and CH_4; therefore, the total STY corresponds to the CO_2 conversion rate, as shown in Fig. S2 (ESI†). For ZnZr46, an increase in the reaction temperature enhances the STY of CH_3OH and CO. At

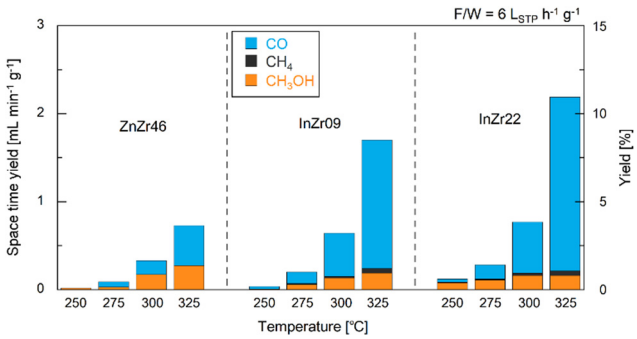

Fig. 1 Space–time yields and yields of CH_3OH, CO, and CH_4 over ZnZr46, InZr09, and InZr22 for CO_2 hydrogenation. F/W = 6 L_{STP} h^{-1} g^{-1}. Pressure = 1.0 MPa. Gas composition: $CO_2/H_2/N_2$ = 1/3/1.

325 °C, the STY of CH_3OH and CO reach 0.27 and 0.46 mL min^{-1} g^{-1}, respectively. CH_4 production is not observed. According to our previous study,[37] we have confirmed that below 400 °C, Zn-doped ZrO_2 produces CH_3OH and CO, but not CH_4. For comparison, we also assessed the performance of commercially available ZnO particles at 325 °C. However, no CH_3OH is observed (Fig. S3a, ESI†). This result indicates that ZnZr46, unlike ZnO, possesses active sites that are effective for CH_3OH production.

In InZr09, the CH_3OH STY is slightly lower than that of ZnZr46, whereas the CO STY is higher (Fig. 1). The increased CO_2 conversion rate (Fig. S2, ESI†) of InZr09 is attributed to the enhanced generation of CO. Additionally, the production of CH_4 is observed. When comparing InZr09 and InZr22, no significant differences are observed in the STY trends. Additionally, the performance of commercially available In_2O_3 is evaluated at 325 °C (Fig. S3a, ESI†). Despite its lower space velocity, the yield of In_2O_3 is lower than that of InZr09 and InZr22, suggesting the presence of additional active sites on InZr09 and InZr22 that activate CO_2. However, these sites are not present in In_2O_3. Notably, In_2O_3 generates CO and CH_3OH while producing a negligible amount of CH_4. Therefore, In_2O_3 does not possess active sites that generate CH_4, whereas InZr09 and InZr22 possess active sites that facilitate CH_4 production.

Structure

In this study, we examined the catalyst structure to reveal the role of active sites. First, we measured the specific surface area (SSA) and total pore volume by N_2 adsorption (Table 1). The SSA of ZnZr46, InZr09, and InZr22 is lower than that of amorphous ZrO_2 (approximately 200 m^2 g^{-1}),[35] which is the raw material. This result was attributed to sintering at 500 °C during catalyst preparation. Fig. 2 shows the high-angle annular dark field scanning transmission electron microscopy (HAADF-STEM) images of ZnZr46, InZr09, and InZr22. Regardless of the catalyst type, all elements are distributed uniformly. The size of the observed particles is approximately 15 nm. Consequently, no differences are observed between the morphologies of the two $InZrO_x$ catalysts.

The crystal structure was examined using X-ray diffraction (XRD) (Fig. 3 and Fig. S3b, ESI†). For amorphous ZrO_2, a broad peak is observed at approximately 31°, indicating a lack of a distinct crystal structure. For ZnZr46, strong peaks are observed at 31°, 35°, and 51°, which correspond to *t*-ZrO_2. In contrast to the conventional anticipation of the formation of monoclinic (*m*-)ZrO_2 from amorphous ZrO_2 at 500 °C, calcination of amorphous ZrO_2 results in the formation of *t*-ZrO_2. This unexpected outcome signifies the incorporation of Zn^{2+} species into the ZrO_2 lattice, leading to the establishment of a solid solution of $ZnZrO_x$ with a tetragonal crystal structure, which agrees with our previously reported observations.[8] The doped Zn^{2+} species coordinated with the O atoms to form isolated [ZnO_a] clusters (refer to ESI† and Fig. S4). The additional peaks at 32°, 34°, 36°, 48°, and 56° indicate the presence of ZnO. Therefore, ZnO precipitates when the Zn/Zr molar ratio exceeds 0.19 because the $ZnZrO_x$ solid solution reaches its limit when additional Zn species are incorporated.[8] Consequently, ZnZr46 contains both

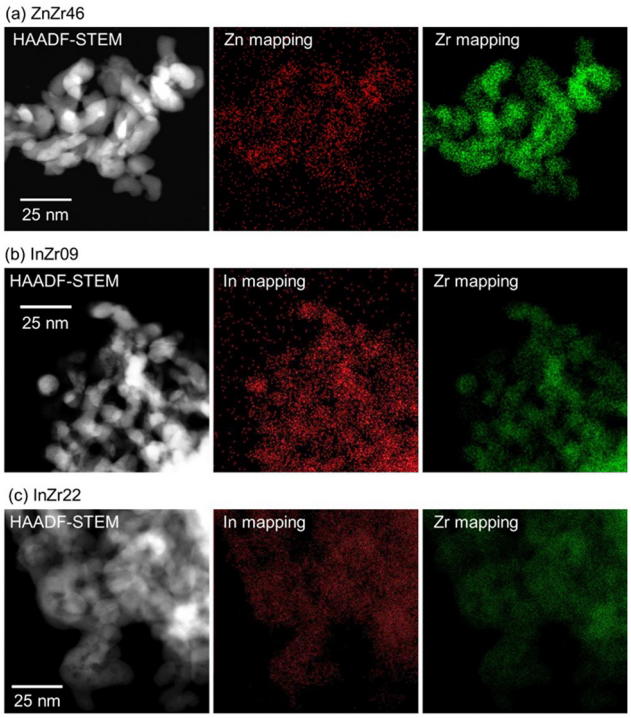

Fig. 2 HAADF-STEM images and elemental maps of (a) ZnZr46, (b) InZr09, and (c) InZr22.

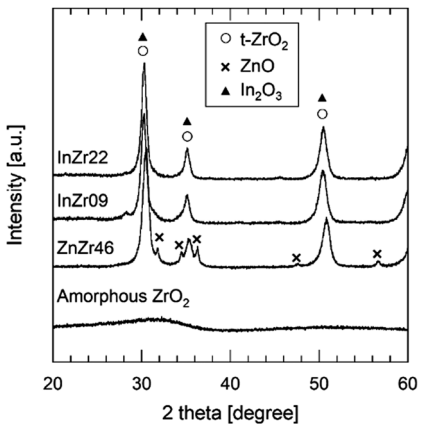

Fig. 3 XRD patterns of amorphous ZrO_2, ZnZr46, InZr09, and InZr22.

the $ZnZrO_x$ solid solution and ZnO. Previous observations indicate minimal differences in catalyst performance among $ZnZrO_x$ samples with different Zn/Zr molar ratios, implying that the [ZnO_a] isolated clusters on the $ZnZrO_x$ solid solution serve as crucial active sites, whereas the ZnO particles remain inert for CO_2 hydrogenation to methanol.[8]

The XRD patterns of InZr09 and InZr22 (Fig. 3) reveal peaks exclusively corresponding to *t*-ZrO_2. The presence of *t*-ZrO_2 instead of *m*-ZrO_2 suggests the incorporation of In species into the ZrO_2 lattice, resulting in the formation of an $InZrO_x$ solid solution. Notably, the peaks derived from tetragonal ZrO_2 and In_2O_3 coincide, making it difficult to unequivocally confirm the

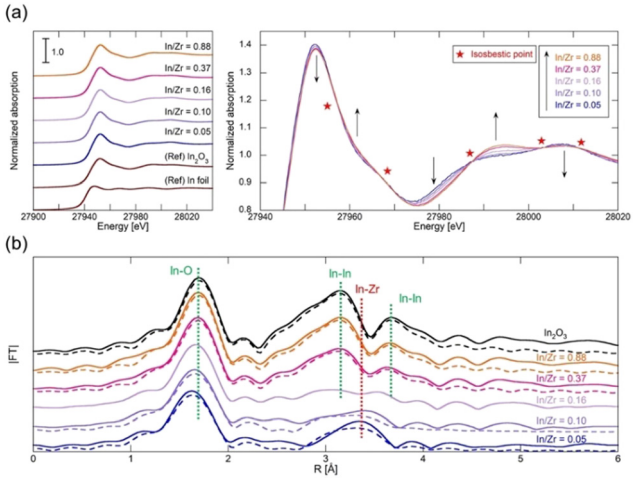

Fig. 4 (a) K-edge XANES spectra of In foil, In_2O_3, and $InZrO_x$ with In/Zr molar ratios of 0.05, 0.10, 0.16, 0.37, and 0.88. (b) Fourier transforms of k^3-weighted extended X-ray absorption fine structure (EXAFS) oscillations measured at room temperature near the In K-edge of $InZrO_x$. k range: 3–12 $Å^{-1}$. R range: 1–4 Å. Solid line: experimental; dotted line: EXAFS model.

existence of In_2O_3 through XRD analysis alone. As elucidated earlier, the presence of the In species is conclusively determined using XRF (Table 1).

We conducted K-edge XAS measurements on various $InZrO_x$ samples with different In/Zr molar ratios (0.05, 0.10, 0.16, 0.37, and 0.88) to explore the structural characteristics of the In species. Our primary focus was to determine the relationship between the In/Zr ratio and coordination structure of In. Fig. 4a shows the In K-edge X-ray absorption near edge structure (XANES) spectra, with In foil and In_2O_3 included as the reference materials. The $InZrO_x$ spectra closely resemble those of In_2O_3, characterized by a distinctive white line at 27 952 eV. A detailed examination of the $InZrO_x$ XANES spectrum reveals several isosbestic points (Fig. 4a), indicating the presence of two distinct In species in $InZrO_x$. The relative proportions of the In species also change with variations in the In : Zr ratio. In Fig. 4b, the In K-edge radial structure functions (RSFs) of In_2O_3 and $InZrO_x$ are shown, and Table 2 summarizes the fitting parameters. The RSF of In_2O_3 exhibits three peaks, representing the nearest-neighbor In–O distance (at 1.7 Å) and the nearest-neighbor and second-nearest In–In distances (at 3.1 and 3.7 Å). For $InZrO_x$ at In/Zr ratios of 0.88 and 0.37, the RSFs exhibit these characteristic peaks. The In–O peaks shift to the left as the ratio decreases from 0.37 to 0.05, indicating a gradual change in the In coordination structure. Simultaneously, the In–In peaks at 3.1 and 3.7 Å gradually disappear, and a new peak emerges at 3.3 Å. The peak at 3.3 Å corresponds to the nearest-neighbor In–Zr distance, determined from the optimized $InZrO_x$ structure (Fig. S1, ESI†). In the sample with an In/Zr ratio of 0.16, the peaks derived from In–In and In–Zr coexist, making it difficult to analyze the coordination structure of the In species by fitting. Consequently, when the In/Zr ratio is low, $InZrO_x$ predominantly contains In^{3+} species doped into t-ZrO_2. Conversely, when the In/Zr ratio is high, $InZrO_x$ primarily contains In_2O_3. These results suggest that the solid solubility limit of the In species is approximately 0.10.

As detailed in the CO_2 hydrogenation section, InZr09 and InZr22 exhibit distinct active sites that are absent in In_2O_3. The catalytic performances of InZr09 and InZr22 are notably similar, as observed for the STYs of CH_3OH, CO, and CH_4 (Fig. 1). XAS measurements (Table 2) further reveal that when the In/Zr ratio is below 0.10, the prevalent In species in $InZrO_x$ are primarily In species doped with t-ZrO_2. Collectively, these findings strongly suggest that the catalytic performances of InZr09 and InZr22 are governed by the presence of doped In species.

Reaction mechanism analysis by DFT

As described earlier, it is evident that the sites responsible for producing CH_3OH and CH_4 are Zn and In species incorporated into ZrO_2. Through DFT calculations, we aimed to delve into reactions at the atomic level, which are challenging to observe experimentally.

Fig. 5 shows the free energy surfaces for CH_4 and CH_3OH formation on the $InZrO_x$ surface. Fig. 6 and 7 show the structures of the reaction intermediates in the formate, CO,

Table 2 Parameters calculated by fitting the EXAFS signals of In_2O_3 and $InZrO_x$ shown in Fig. 4b

Sample	Path	CN	σ^2 [Å]	ΔE_0 [eV]	R [Å]	R factor
In_2O_3	In–O	5.5 ± 0.3	0.007 ± 0.001	8.0 ± 0.7	2.16 ± 0.01	0.002
	In–In	5.1 ± 0.8	0.005 ± 0.001	7.0 ± 0.9	3.35 ± 0.01	
	In–In	3.8 ± 1.2	0.005 ± 0.002	7.2 ± 1.9	3.84 ± 0.01	
$InZrO_x$						
In/Zr = 0.88	In–O	6.2 ± 0.5	0.007 ± 0.001	7.2 ± 0.9	2.16 ± 0.01	0.003
	In–In	5.2 ± 1.2	0.006 ± 0.001	5.8 ± 1.4	3.36 ± 0.01	
	In–In	3.6 ± 1.8	0.006 ± 0.003	6.2 ± 3.1	3.83 ± 0.02	
In/Zr = 0.37	In–O	6.1 ± 0.4	0.007 ± 0.001	6.8 ± 0.7	2.16 ± 0.01	0.003
	In–In	4.3 ± 0.9	0.006 ± 0.001	5.0 ± 1.3	3.36 ± 0.01	
	In–In	2.7 ± 1.3	0.005 ± 0.003	4.9 ± 3.0	3.83 ± 0.02	
In/Zr = 0.10	In–O	5.0 ± 0.7	0.007 ± 0.001	7.5 ± 1.6	2.14 ± 0.01	0.034
	In–Zr	8.1 ± 3.8	0.017 ± 0.004	5.2 ± 2.8	3.53 ± 0.02	
In/Zr = 0.05	In–O	4.5 ± 0.5	0.007 ± 0.001	6.2 ± 1.4	2.12 ± 0.01	0.022
	In–Zr	6.7 ± 2.1	0.013 ± 0.002	6.4 ± 2.1	3.57 ± 0.02	

Notation: CN, coorination number; σ, Debye–Waller factor; ΔE_0, increase in the threshold energy; R, distance. Confidence intervals = 68%.

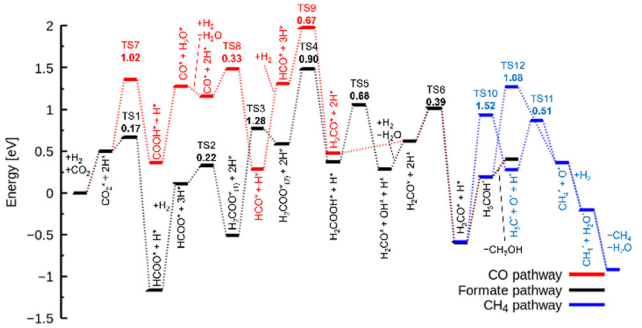

Fig. 5 Free energy surfaces of the $InZrO_x$ surface for formate (black), CO (red), and CH_4 (blue) pathways. The values in the bold face and * indicate the activation free energies of the TSs and adsorbed species, respectively.

and CH_4 pathways, respectively. Fig. S5 (ESI†) shows the structures of transition states (TSs) in Fig. 5.

In the formate pathway, CO_2 adsorbs onto the surface Zr atoms as a bidentate carbonate species, whereas H_2 dissociates and adsorbs onto the surface Zr and O atoms. The adsorbed CO_2 is protonated by the neighboring H atom to form HCOO (formate). The formate group receives a H atom to form H_2COO. One O atom in H_2COO changes its bond with the surface Zr atom to an In atom with the largest barrier ($\Delta G^{\ddagger}$) of 1.28 eV in the formate pathway. The O atom on the In atom in H_2COO accepts the H atom to form H_2COOH, which then decomposes into H_2CO (formaldehyde), OH, and H species. Protonation of formaldehyde yields a methoxy group (H_3CO), which is converted into CH_3OH by further protonation.

In the CO pathway, the H atom on the In atom hydrogenates adsorbed CO_2 to yield COOH (carboxyl group). This carboxyl group decomposes into CO and water. The CO molecule successively changes to HCO, H_2CO (formaldehyde) and finally, to H_3CO to join the formate pathway. In Fig. 1, CO production increases at higher temperatures partly because CO_2 hydrogenation to CH_3OH is an exothermic reaction while the reverse water gas shift reaction is an endothermic reaction, making the chemical equilibrium shift to the right side in $CO_2 + H_2 \rightleftarrows CO + H_2O$ and enhancing CO production at higher reaction temperatures. However, it is noted that we showed in Fig. S6 (ESI†) by changing the space velocity that CH_3OH can be converted to CO, contributing to CO production. Fig. 5 shows that the decomposition of COOH to CO and H_2O, which undergoes also at zirconia surfaces,[38] is endothermic by 0.92 eV, and it is found to be barrierless. This suggests that after CO is formed from the decomposition of COOH, the backward reaction can proceed without a barrier, allowing CO to readily transition back to a stable COOH. Additionally, the adsorption energy in Table S1 (ESI†) is the highest for a CO molecule among the reaction intermediates. This indicates that a CO molecule can desorb from the catalyst surface easier than the other intermediates,[7] and the CO pathway does not proceed further.

In the CH_4 pathway, Fig. 5 suggests two possible routes: decompositions of methoxy group and CH_3OH. In the case of methoxy group decomposition, the methyl group in the methoxy group is transferred to the surface of the In atom for stable adsorption, with a C–In distance of 2.69 Å. However, this adsorption is unstable on the Zn atom of the $ZnZrO_x$ surface, and the methyl group changes to a methoxy group (Fig. S7, ESI†) because the methyl group forms a bond with the O atom next to Zn. The barrier of the methyl group transfer is 1.52 eV on the $InZrO_x$ surface, which is higher than those in the other steps of this study, such as 1.28 eV in the formate pathway. It is also higher than those in CH_3OH formation from CO_2 on $ZnZrO_x$ surfaces.[7,31] This suggests that CH_4 production is unfavored compared to CH_3OH. This result is consistent with the lower experimental yield of CH_4 than that of CH_3OH. Therefore, methyl group transfer is the rate-determining step in CH_4 formation. This result supports the experimental evidence of CH_4 formation on the $InZrO_x$ surface, indicating that stable adsorption of a methyl group on the $InZrO_x$ surface is important for CH_4 production.

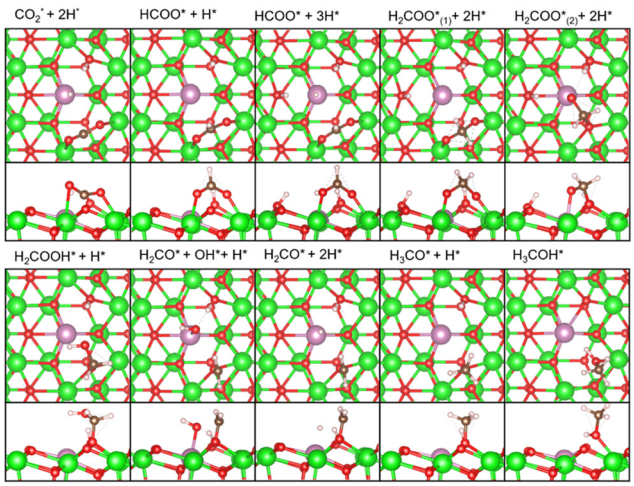

Fig. 6 Top and side views of the reaction intermediates in the formate pathway of Fig. 5. Color code: green: Zr, red: O, purple: In, white: H, and brown: C. The figures are made by VESTA.[39]

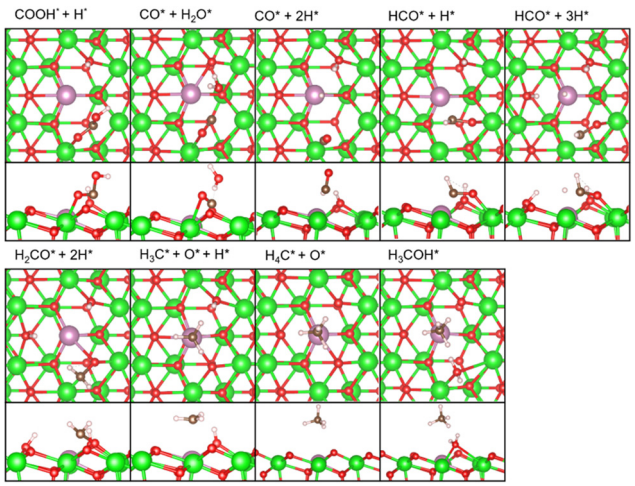

Fig. 7 Top and side views of the reaction intermediates in the CO and CH_4 pathways in Fig. 5. Color code: green: Zr, red: O, purple: In, white: H, and brown: C. The figures are made by VESTA.[39]

The methyl group adsorbed on the In atom accepts a proton from the neighboring OH group to form CH_4. The remaining O atom adsorbed at the V_O site combines with the H_2 molecule to form H_2O. The H_2O and CH_4 molecules finally desorb from the surface into the gas phase, completing CH_4 formation. In the last step, the $InZrO_x$ surface regains the surface V_O sites.

In the case of CH_3OH decomposition ($CH_3OH \rightarrow CH_4 + O^*$) without the transfer of the methyl group on the $InZrO_x$ surface, the activation free energy is 1.08 eV that is lower than that in the case of methoxy group decomposition, yet CH_3OH desorbs with the free energy difference of only 0.21 eV. This suggests that CH_3OH decomposition can be competitive but is unfavored over CH_3OH desorption. It is noted that the decomposition of a CH_3OH molecule on the $ZnZrO_x$ surface requires a higher barrier (2.60 eV) as illustrated in Fig. S8 (ESI†), indicating that CH_4 production on the $ZnZrO_x$ surface is unfavored.

Here, we discuss the density of states (DOS) shown in Fig. 8 to understand the adsorption of methyl groups on the $InZrO_x$ surface. The mid-gap (also called the impurity) band for the $InZrO_x$ surface in Fig. 8a lies between the valence band maximum of ZrO_2 and the conduction band minimum. The mid-gap band primarily arises from the In atom, and the *s* and $5p_z$ orbitals mainly contribute to the DOS of the In atom, as shown in Fig. 8d (the *z* coordinate is along the surface-normal direction). In contrast, the DOS of the $ZnZrO_x$ surface in Fig. 8b has no midgap band. The *d* band of a Zn atom in Fig. 8e dominates the DOS of the Zn atom between −10 and 0 eV.

The projected DOSs of In and C atoms on the $InZrO_x$ surface with an adsorbed methyl group in Fig. 8c also shows a mid-gap state. Fig. 8f shows the midgap state consisting of the $5p_z$ orbital of the In atom and $2p_z$ orbital of the C atom. Therefore, the $5p_z$ orbital of the In atom and the $2p_z$ orbital of the C atom overlapped with the adsorbed methyl group on the $InZrO_x$ surface, and the distinct band structures of the doped metals determined the adsorption strength of the methyl group on the $InZrO_x$ and $ZnZrO_x$ surfaces. A methyl group was readily adsorbed on the In atom on the $InZrO_x$ surface owing to the superior overlap of orbitals; however, the adsorption of a methyl group on the Zn atom on the $ZnZrO_x$ surface is unstable, as shown in Fig. S7 (ESI†). Therefore, In-doping of ZrO_2 enhances CH_4 formation.

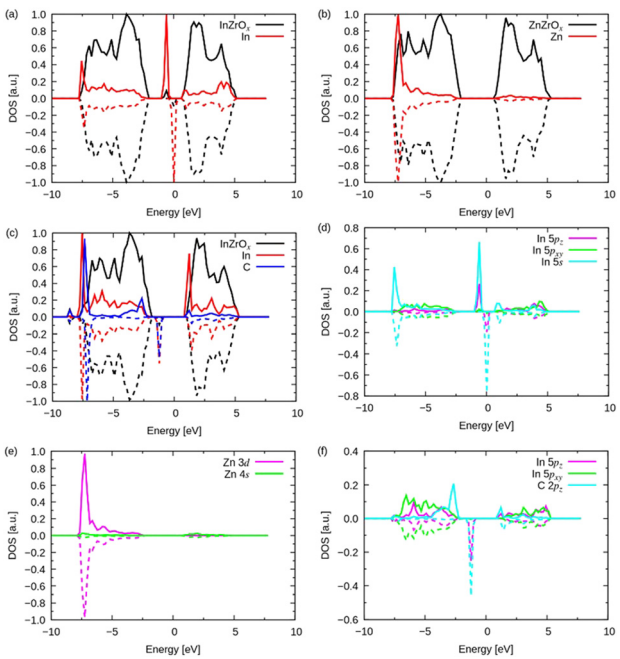

Fig. 8 Density of states (DOS) of neat (a) $InZrO_x$, (b) $ZnZrO_x$ surfaces, and (c) methyl groups on the $InZrO_x$ surface. The solid and dashed lines denote the up and down spins, respectively. Each DOS is normalized for clarity. (d)–(f) Projected DOSs corresponding to panels (a)–(c), where the *z* coordinate is along the surface normal direction.

CH_3OH conversion

We conducted a test of the CH_3OH conversion reaction to directly observe how each catalyst activates the CH_3OH molecules (Fig. 9). Taking into consideration the reaction condition of CO_2 hydrogenation, unreacted H_2 is assumed to coexist with CH_3OH during CO_2 hydrogenation. Hence, for the CH_3OH conversion test, CH_3OH and H_2 were supplied simultaneously.

ZnZr46 generates CO and CH_3OCH_3 from CH_3OH. The former is attributed to the product of the CH_3OH decomposition reaction, which represents the reverse of the CH_3OH synthesis *via* CO hydrogenation (eqn (3)). In contrast, the latter is related to CH_3OH dehydration (eqn (10)) at the Brønsted acid site of the catalyst.

$$2CH_3OH \rightarrow CH_3OCH_3 + H_2O \qquad (10)$$

Apart from ZrO_2, which possesses acid sites, Brønsted acid sites are formed by doping metal into ZrO_2.[40] Moreover, the CH_4 production is minimal, with a selectivity below 1%. Even when using commercially available ZnO, the CO selectivity (93%) is much higher than that for CH_4 (3%) and CH_3OCH_3 (4%). For InZr22, along with CO and CH_3OCH_3, a significant amount of CH_4 is generated (selectivity = 15%). Notably, the results for In_2O_3 revealed a CH_4 selectivity of 65%, although the

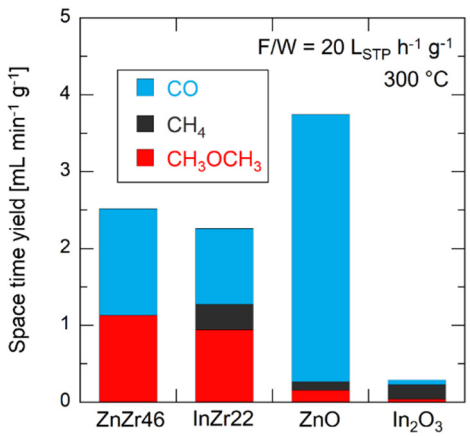

Fig. 9 Space time yields of CO, CH_4, and CH_3OCH_3 over ZnZr46, InZr22, ZnO, and In_2O_3 for the methanol conversion reaction. F/W = 20 L_{STP} h^{-1} g^{-1}. Temperature = 300 °C. Pressure = 0.1 MPa. Gas composition: $CH_3OH/H_2/N_2$ = 13/22/65.

yield is extremely small compared to that of the other catalysts. These results align with the computational chemistry predictions, indicating that CH_3OH is directly converted to CH_4 on In^{3+}. As shown in Fig. S3 (ESI†), during the CO_2 hydrogenation reaction with In_2O_3, CH_3OH is observed, but CH_4 remains undetected. Therefore, the results in Fig. S3 (ESI†) and Fig. 9 appear to be contradictory. We expect that the absence of CH_4 in the CO_2 hydrogenation reaction with In_2O_3 is linked to the inhibition of the In-methoxy bond formation owing to the presence of CO_2 in the reaction gas. However, we were unable to clarify these differences beyond the reaction tests. We plan to explore and elucidate this distinction in future studies.

Conclusions

This study focused on oxide solid-solutions of $ZnZrO_x$ and $InZrO_x$ for CO_2-to-CH_3OH hydrogenation and clarified the differences in their reaction mechanisms. For both catalysts, the metal cations (In^{3+} and Zn^{2+}) incorporated into the *t*-ZrO_2 lattice serve as crucial active sites for CH_3OH synthesis. In the case of the $ZnZrO_x$ catalyst, CO is produced as a byproduct along with CH_3OH. Conversely, the $InZrO_x$ catalyst produces a small amount of CH_4, in addition to CH_3OH and CO. Remarkably, CH_4 is produced by passing CH_3OH and H_2 through the $InZrO_x$ catalyst. We performed a DFT study on CH_4 formation on $InZrO_x$ by calculating the free energy surface and density of states (DOS). Our calculations suggest a possible reaction pathway, highlighting the methyl group transfer with a competitive activation barrier, which is consistent with the experimental findings. The CH_3OH decomposition was also suggested to contribute to the CH_4 production. A methyl group can only be adsorbed on the $InZrO_x$ catalyst due to the better overlap of DOS between the adsorbate and substrate than on the $ZnZrO_x$ catalyst.

Author contributions

This manuscript was written through the contributions of all authors. All authors have given approval to the final version of the manuscript.

Conflicts of interest

There are no conflicts of interest to declare.

Acknowledgements

This study was financially supported by the Feasibility Study Program on Energy and New Environmental Technology (No. 22100386-0) of the New Energy and Industrial Technology Development Organization of Japan, the JSPS KAKENHI (Grant Number 24K01240), and the Environment Research and Technology Development Fund (JPMEERF20243RA3) of the Environmental Restoration and Conservation Agency provided by Ministry of the Environment of Japan. We thank the Advanced Research Infrastructure for Materials and Nanotechnology of Japan (ARIM) program (Grant No. JPMXP1222OS0026) from the Ministry of Education, Culture, Sports, Science, and Technology (MEXT), Japan, at the Research Center for Ultra-High-Voltage Electron Microscopy (Nanotechnology Open Facilities), Osaka University. Synchrotron radiation experiments were performed at BL14B2 of SPring-8 with the approval of the Japan Synchrotron Radiation Research Institute (JASRI, Proposal no. 2023B1576). We used supercomputers from the Institute for Solid State Physics, University of Tokyo, ACCMS, Kyoto University, and the Research Institute for Information Technology, Kyushu University.

References

1 M. Behrens, F. Studt, I. Kasatkin, S. Kuhl, M. Hävecker, F. Abild-Pedersen, S. Zander, F. Girgsdies, P. Kurr, B. L. Kniep, M. Tovar, R. W. Fischer, J. K. Nørskov and R. Schlögl, *Science*, 2012, **336**, 893–897.
2 S. Kuld, M. Thorhauge, H. Falsig, C. F. Elkjaer, S. Helveg, I. Chorkendorff and J. Sehested, *Science*, 2016, **352**, 969–974.
3 S. Kattel, P. J. Ramirez, J. G. Chen, J. A. Rodriguez and P. Liu, *Science*, 2017, **355**, 1296–1299.
4 M. Stöcker, *Microporous Mesoporous Mater.*, 1999, **29**, 3–48.
5 A. Alvarez, A. Bansode, A. Urakawa, A. V. Bavykina, T. A. Wezendonk, M. Makkee, J. Gascon and F. Kapteijn, *Chem. Rev.*, 2017, **117**, 9804–9838.
6 S. Tada, H. Kinoshita, N. Ochiai, A. Chokkalingam, P. Hu, N. Yamauchi, Y. Kobayashi and K. Iyoki, *Int. J. Hydrogen Energy*, 2021, **46**, 36721–36730.
7 J. J. Wang, G. N. Li, Z. L. Li, C. Z. Tang, Z. C. Feng, H. Y. An, H. L. Liu, T. F. Liu and C. Li, *Sci. Adv.*, 2017, **3**, e170129.
8 S. Tada, N. Ochiai, H. Kinoshita, M. Yoshida, N. Shimada, T. Joutsuka, M. Nishijima, T. Honma, N. Yamauchi, Y. Kobayashi and K. Iyoki, *ACS Catal.*, 2022, **12**, 7748–7759.
9 Z. Feng, C. Tang, P. Zhang, K. Li, G. Li, J. Wang, Z. Feng and C. Li, *J. Am. Chem. Soc.*, 2023, **145**, 12663–12672.
10 K. Y. H. Lee, U. Anjum, C. Mondelli, Q. He, S. Furukawa, J. Perez-Ramirez, S. M. Kozlov, N. Yan and T. P. Araujo, *Appl. Catal., B*, 2022, **304**, 120994.
11 K. Fujiwara, T. Akutsu, M. Nishijima and S. Tada, *Top. Catal.*, 2023, **66**, 1492–1502.
12 T. P. Araujo, J. Morales-Vidal, T. Zou, M. Agrachev, S. Verstraeten, P. O. Willi, R. N. Grass, G. Jeschke, S. Mitchell, N. Lopez and J. Perez-Ramirez, *Adv. Energy Mater.*, 2023, **13**, 2204122.
13 C. Temvuttirojn, Y. Poo-arporn, N. Chanlek, C. K. Cheng, C. C. Chong, J. Limtrakul and T. Witoon, *Ind. Eng. Chem. Res.*, 2020, **59**, 5525–5535.
14 T. P. Araujo, J. Morales-Vidal, G. Giannakakis, C. Mondelli, H. WEliasson, R. Erni, J. Stewart, S. Mitchell, N. Lopez and J. Perez-Ramirez, *Angew. Chem., Int. Ed.*, 2023, **62**, e202306563.
15 J. Wang, G. Zhang, J. Zhu, X. Zhang, F. Ding, A. Zhang, X. Guo and C. Song, *ACS Catal.*, 2021, **11**, 1406–1423.

16 M. S. Frei, C. Mondelli, R. Garcia-Muelas, K. S. Kley, B. Puertolas, N. Lopez, O. V. Safanova, J. A. Stewart, D. C. Ferre and J. Perez-Ramirez, *Nat. Commun.*, 2019, **10**, 3377.
17 J. J. Wang, C. Z. Tang, G. N. Li, Z. Han, Z. L. Li, H. Liu, F. Cheng and C. Li, *ACS Catal.*, 2019, **9**, 10253–10259.
18 J. Ye, C. Liu, D. Mei and Q. Ge, *ACS Catal.*, 2013, **3**, 1296–1306.
19 O. Martin, A. J. Martin, C. Mondelli, S. Mitchell, T. F. Segawa, R. Hauert, C. Drouilly, D. Curulla-Ferre and J. Perez-Ramirez, *Angew. Chem., Int. Ed.*, 2016, **55**, 6261–6265.
20 M. S. Frei, C. Mondelli, R. García-Muelas, K. S. Kley, B. Puértolas, N. López, O. V. Safonova, J. A. Stewart, D. C. Ferré and J. Pérez-Ramírez, *Nat. Commun.*, 2019, **10**, 3377.
21 A. Posada-Borbón and H. Grönbeck, *ACS Catal.*, 2021, **11**, 9996–10006.
22 S. Tada and K. Iyoki, *Chem. Lett.*, 2021, **50**, 724–726.
23 S. Tada and R. Kikuchi, *Catal. Sci. Technol.*, 2015, **5**, 3061–3070.
24 M. Marwood, R. Doepper and A. Renken, *Appl. Catal., A*, 1997, **151**, 223–246.
25 Y. Xie, J. Chen, X. Wu, J. Y. Wen, R. Zhao, Z. Li, G. Tian, Q. Zhang, P. Ning and J. Hao, *ACS Catal.*, 2022, **12**, 10587–10602.
26 G. Kresse and J. Furthmüller, *Phys. Rev. B: Condens. Matter Mater. Phys.*, 1996, **54**, 11169–11186.
27 G. Kresse and J. Furthmüller, *Comput. Mater. Sci.*, 1996, **6**, 15–50.
28 G. Kresse and D. Joubert, *Phys. Rev. B: Condens. Matter Mater. Phys.*, 1999, **59**, 1758–1775.
29 J. P. Perdew, K. Burke and M. Ernzerhof, *Phys. Rev. Lett.*, 1996, **77**, 3865–3868.
30 M. Delarmelina, M. G. Quesne and R. A. Catlow, *Phys. Chem. Chem. Phys.*, 2020, **22**, 6660–6676.
31 S. L. Zhou and S. Li, *J. Phys. Chem. C*, 2020, **124**, 27467–27478.
32 H. J. Monkhorst and J. D. Pack, *Phys. Rev. B: Solid State*, 1976, **13**, 5188–5192.
33 J. Neugebauer and M. Scheffler, *Phys. Rev. B: Condens. Matter Mater. Phys.*, 1992, **46**, 16067–16080.
34 F. Haase and J. Sauer, *J. Am. Chem. Soc.*, 1998, **120**, 13503–13512.
35 T. Joutsuka and S. Tada, *J. Phys. Chem. C*, 2023, **127**, 6998–7008.
36 G. Henkelman and H. Jonsson, *J. Chem. Phys.*, 2000, **113**, 9978–9985.
37 S. Tada, H. Kinoshita, D. Li, M. Nishijima, H. Yamaguchi, R. Kikuchi, N. Yamauchi, Y. Kobayashi and K. Iyoki, *Adv. Powder Technol.*, 2023, **34**, 104174.
38 M. E. Kauppinen, M. M. Melander, A. S. Bazhenov and K. Honkala, *ACS Catal.*, 2018, **8**, 11633–11647.
39 K. Momma and F. Izumi, *J. Appl. Crystallogr.*, 2011, **44**, 1272–1276.
40 C. A. Akinnawo, N. Bingwa and R. Meijboom, *New J. Chem.*, 2021, **45**, 7878–7892.